IEEE Access
Multidisciplinary | Rapid Review | Open Access Journal

Received 20 September 2023, accepted 24 November 2023, date of publication 28 November 2023,
date of current version 5 December 2023.

Digital Object Identifier 10.1109/ACCESS.2023.3337444

RESEARCH ARTICLE

A Plane Wave Equivalent Model for Forward Scatter Shadow Ratio in Spherical Wave and Its Application in Shadow Profile Retrieval

XI SHEN, (Member, IEEE), AND DEFENG HUANG, (Senior Member, IEEE)
Department of Electrical, Electronic and Computer Engineering, The University of Western Australia, Perth, WA 6009, Australia
Corresponding author: Defeng Huang (david.huang@uwa.edu.au)

This work was supported in part by the Australian Research Council (ARC) under Grant DP220101894.

ABSTRACT The forward scatter shadow ratio (FSSR), a novel parameter in forward scatter radar (FSR) systems, has been introduced recently for a plane wave. In contrast to conventional parameters like the forward scatter cross section (FSCS), FSSR utilizes the total electric field, providing a direct indicator of signal deviations from the direct path. This study overcomes the limitations of the current FSSR model by conducting a comprehensive mathematical and numerical analysis for a spherical wave with the Kirchhoff diffraction formula. By incorporating a point source and moving targets, this approach extends the application scope of FSSR. A plane wave equivalent model is derived and compared to the point source model, demonstrating its accuracy in various scenarios. The optimization method for target shadow profile retrieval in moving targets is discussed using the plane wave equivalent model. It is suggested that employing dual receivers can eliminate the ambiguity associated with target localization and enhance shadow profile retrieval precision.

INDEX TERMS Forward scatter radar, forward scatter shadow ratio, shadow profile, diffraction.

I. INTRODUCTION

Recently, a new parameter to describe the target in the forward scatter radar (FSR) system with a plane wave as the signal source, namely the forward scatter shadow ratio (FSSR), was introduced [1], [2], [3]. As a parameter relevant to target detection, size estimation, classification and shadow profile imaging, FSSR is defined as the ratio of the total received power density to the direct path signal (DPS) power density. Differing from the commonly used parameter of forward scatter cross section (FSCS) [4], [5], which is adopted from the concept of radar cross-section (RCS) in mono or traditional bistatic radar, FSSR uses the total electric field rather than the forward scatter radiation, and is a direct indicator of how far the total received signal deviates from the DPS. Unlike FSCS, using FSSR doesn't require the removal of the DPS, which is especially challenging in cases involving passive illuminators of opportunity (IOs) [6], [7], [8].

The associate editor coordinating the review of this manuscript and approving it for publication was Guido Lombardi.

We have proposed that FSSR can be used for target shadow profile retrieval through an optimization method. Represented by a finite number of rectangular strips, the target shadow profile can be retrieved using discrete observations of FSSR [1], [2]. Compared to SISAR [9], this approach only discretizes the target using rectangular strips but without any further approximation. It is able to retrieve both the upper and lower limits of the strips (as opposed to heights only in SISAR). Furthermore, it is based on an optimization method and thus can easily accommodate FSSR samples from different locations.

There are two main limitations with the current investigations on FSSR and its application in target shadow profile retrieval. Firstly, the current definition of FSSR is given in a model where the incident signal is assumed a plane wave. The general scenario for a realistic FSR system where the DPS is from a point source is still to be investigated. Secondly, the current analyses of FSSR are based on the Fresnel diffraction formula [10], which is an approximation of the Rayleigh-Sommerfeld diffraction formula when the

© 2023 The Authors. This work is licensed under a Creative Commons Attribution 4.0 License.
For more information, see https://creativecommons.org/licenses/by/4.0/

range of observation is large compared to the target size. An analysis with the Kirchhoff diffraction formula, in line with the existing studies of SISAR [11], [12], [13], is needed.

This paper extends the definition of FSSR to spherical wave, i.e., the transmitter is regarded as a point source. Furthermore, FSSR is analyzed using the Kirchhoff diffraction formula, in which the target is moving across the transmitter-receiver baseline. A comparison between the model using the Fresnel formula and that using the Kirchhoff formula is given, and a plane wave equivalent model for the point source model is derived. Let D_1 and D_2 be the distances from the target's projection on the baseline to the point source and to the receiver, respectively, the plane wave equivalent model can be summarized as follows:

$$R = \frac{D_1 D_2}{D_1 + D_2}, \tag{1}$$

where R is the distance between the target and the receiver in an equivalent system with a plane wave as the signal source, under the condition that both the target's dimension and its distance from the baseline are significantly smaller than D_1 and D_2. Using numerical analysis, it is shown that the plane wave equivalent model generates very marginal errors for both the far-field and the close to near-field scenarios. With the plane wave equivalent model, the existing conclusions using the Fresnel diffraction formula can be applied to FSR systems with a point source.

The optimization method for target shadow profile retrieval is discussed within the framework of the new model in which the target is moving across the baseline. The target shadow profile, represented by a finite number of rectangular strips, is retrieved using discrete observations of the FSSR. The plane wave equivalent model is applied to enable the utilization of the nonlinear least-squares algorithm [2]. Different targets with various sizes and shapes are used to examine the shadow profile retrieval capability of the proposed method under both far-field and close to near-field scenarios. The numerical results indicate that using two receivers instead of one helps eliminate the ambiguity in locating the target and improves the accuracy of target shadow profile retrieval.

The rest of this paper is organized as follows. The FSSR model based on the Kirchhoff diffraction formula is described in Section II. In Section III, the plane wave equivalent model is derived and then analyzed numerically. The optimization method for target shadow profile retrieval with one and two receivers is described and then numerically analyzed in Section IV. Finally, Section V concludes this paper.

II. FSSR IN SPHERICAL WAVE

Consider a forward scatter scenario shown in Fig. 1, where a target is in close proximity to the baseline that connects the transmitter (TX) with the receiver (RX). The TX is a point source of a spherical wave. This spherical wave model is the same as that used in SISAR [9]. Note that the model with a plane wave closely resembles the spherical wave propagation when the source is far away from the target [2]. With the distance from the source to the target taken into account, the spherical wave model offers a higher level of accuracy.

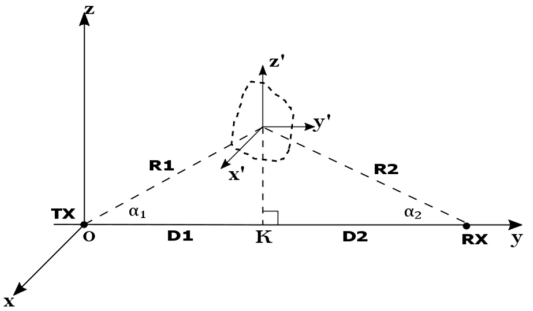

FIGURE 1. An illustration of an idealized forward scatter radar system.

TABLE 1. Normalized values of distances and dimensions.

Normalized Value: D/x' / λ	D or R		x, z, x' or z'	
	1 km	10 km	0.2 m	1 m
$\lambda = 1$ cm	1×10^5	1×10^6	20	100
$\lambda = 5$ cm	2×10^4	2×10^5	4	20

Consider a Cartesian system with the transmitter at the origin and the baseline on the y-axis, as shown in Fig. 1. A second Cartesian system with target's center at its origin is also established, with axes x', y' and z' in the same direction with axes x, y and z, respectively. For simplicity, the target is considered crossing the baseline perpendicularly and the point of intersection is at point K, which is D_1 from the transmitter and D_2 from the receiver. The FSSR (ε) of a target for specific locations of the transmitter and the receiver is the ratio of the total received power density (P_{tot}) to the power density (P_{inc}) of the direct path signal (DPS) measured at the receiver:

$$\varepsilon(D_1, D_2) = \frac{P_{tot}(D_1, D_2)}{P_{inc}(D_1, D_2)} = \frac{\left|E_{tot}(D_1, D_2)\right|^2}{\left|E_{inc}(D_1, D_2)\right|^2}, \tag{2}$$

in which E_{tot} and E_{inc} are the complex amplitudes of the total electric field and the direct path electric field at the receiver, respectively. Note that this definition is compatible with that in the plane wave introduced in [2] and [3]. The total electric field is the outcome of the incident electric field interfering with the forward scattering field caused by the target.

Using Babinet's principle and replacing the target with a complementary aperture that has the shape of the target shadow silhouette on the $x'-z'$ plane, we can apply the Kirchhoff diffraction formula [10] and obtain the complex amplitude of the diffraction field E_D when the target is located at (x, D_1, z):

$$E_D(D_1, D_2, x, z) = \frac{-i}{2\lambda} \iint F(x', z') \frac{e^{2\pi i(R_1+R_2)}}{R_1 R_2} (\cos\alpha_1 + \cos\alpha_2) dx' dz' \tag{3}$$

where the imaginary unit is denoted by i, the wavelength of the signal is denoted by λ, and D_1, D_2, R_1, R_2, x, z, x' and

z' are all normalized with respect to the wavelength, so they are dimensionless. Some examples of the normalized value for different wavelengths can be found in Table 1.

The aperture function $F\left(x', z'\right)$ is given by

$$F\left(x', z'\right) = \begin{cases} 1, & \{x', z'\} \in \Sigma \\ 0, & \text{otherwise} \end{cases} \tag{4}$$

where Σ is the target shadow silhouette on the $x' - z'$ plane, and

$$R_1 = \sqrt{D_1^2 + (x + x')^2 + (z + z')^2}, \tag{5}$$

$$R_2 = \sqrt{D_2^2 + (x + x')^2 + (z + z')^2}. \tag{6}$$

The complex amplitude of the direct path electric field is

$$E_{inc}(D_1, D_2) = \frac{1}{(D_1 + D_2)\lambda} e^{2\pi i(D_1+D_2)}. \tag{7}$$

Finally, the complex amplitude of the total electric field is given by

$$E_{tot} = E_{inc} - E_D. \tag{8}$$

Although both the expressions for the diffraction field in (3) and the direct path electric field in (7) have wavelength λ in them, from (2) we can see that λ will no longer exist in the ratio of FSSR. From (2) to (8), it can be concluded that FSSR is not only affected by the target shadow silhouette, but also the locations of the transmitter, the receiver and the target. Due to the forward scattering field from a target interfering with the DPS, FSSR deviates from one and changes in value while the target changes position with respect to the transmitter and the receiver. If a series of FSSR samples are measured at the receiver, they can potentially be used for target detection, classification, size estimation and shadow profile imaging. In Fig. 2, the numerically calculated FSSRs on a plane perpendicular to the baseline for two different scenarios are shown. In Fig. 2(a), the target is a 180 by 120 rectangle, which is on a plane 2×10^5 from the transmitter, and in Fig. 2(b), the target is a circle of diameter 100, and on a plane 3×10^5 from the transmitter. In both cases the transmitter and the receiver are 4×10^5 apart.

III. PLANE WAVE EQUIVALENT MODEL FOR FSSR IN SPHERICAL WAVE

In previous studies, the Fresnel diffraction formula [3] for a plane incident wave was used for the FSSR definition, where the FSR system in Fig. 3 was considered. The Cartesian system is defined where the receiver is on the y-axis and the incident wave is in the direction of the y-axis. The projection of the target's center on the y-axis is the origin. The Cartesian system of $x' - y' - z'$ is defined the same way as that in Fig. 1. The diffraction field for the target at $(x, 0, z)$ and the receiver at $(0, R, 0)$ is given by

$$E_D(x, z, R) = \frac{e^{2\pi Ri}}{iR} \iint F\left(x', z'\right) e^{\frac{\pi i}{R}[(x+x')^2+(z+z')^2]} dx'dz' \tag{9}$$

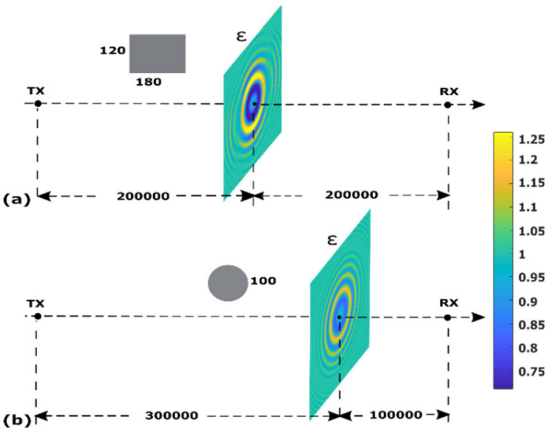

FIGURE 2. The numerically calculated FSSRs for a plane perpendicular to the baseline for: (a) a 180 by 120 rectangular target on a plane 200,000 from the transmitter, (b) a circular target of diameter 100 on a plane 300,000 from the transmitter. The receiver is 400,000 from the transmitter for both cases.

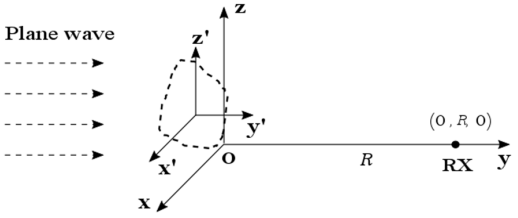

FIGURE 3. An illustration of the forward scatter model where the Fresnel diffraction formula is used.

in which x, z, x' and z' are also all normalized with respect to the wavelength. The expression of the diffraction field in (9) is simpler than that in (3), and wavelength λ is eliminated in (9). Furthermore, from (2), (8) and (9), the FSSR is given by [2]:

$$\varepsilon = \left| 1 - \frac{1}{iR} \iint F\left(x', z'\right) e^{\frac{\pi i}{R}[(x+x')^2+(z+z')^2]} dx'dz' \right|^2. \tag{10}$$

A. THE PLANE WAVE EQUIVALENT MODEL

First of all, we approximate (3) as follows:

$$E_D(D_1, D_2, x, z) \approx \frac{-i}{\lambda} \iint F\left(x', z'\right) \frac{e^{2\pi i(R_1+R_2)}}{R_1 R_2} dx'dz' \tag{11}$$

under the condition that

$$(\cos\alpha_1 + \cos\alpha_2) \approx 2, \tag{12}$$

which can be interpreted as

$$\frac{L}{D} \ll 1, \tag{13}$$

where L is the longest distance from any point described by $F\left(x', z'\right)$ to the baseline and D is the lesser of D_1 and D_2. In other words, compared with its distances to the transmitter and the receiver, both the target's dimension and its distance

from the baseline are significantly smaller. From (8) and (11) we can obtain

$$E_{tot} = E_{inc} - E_D = \frac{1}{(D_1 + D_2)\,\lambda} e^{2\pi i(D_1+D_2)} + \frac{i}{\lambda} \iint F\left(x', z'\right) \frac{e^{2\pi i(R_1+R_2)}}{R_1 R_2} dx' dz'. \tag{14}$$

From (2) and (14), FSSR is given by

$$\varepsilon = \left|\frac{E_{tot}}{E_{inc}}\right|^2 = \left|1 + \frac{(D_1 + D_2)\,i}{e^{2\pi i(D_1+D_2)}} \iint F\left(x', z'\right) \frac{e^{2\pi i(R_1+R_2)}}{R_1 R_2} dx' dz'\right|^2 \tag{15}$$

Note that the condition in (13) can also lead to the second approximation:

$$\frac{1}{R_1 R_2} \approx \frac{1}{D_1 D_2} \tag{16}$$

So (15) becomes

$$\varepsilon \approx \left|1 + \frac{(D_1 + D_2)\,i}{D_1 D_2} e^{-2\pi i(D_1+D_2)} \times \iint F\left(x', z'\right) e^{2\pi i(R_1+R_2)} dx' dz'\right|^2 \tag{17}$$

We substitute R_1 and R_2 with (5) and (6), and make the third approximation as:

$$\sqrt{D_1^2 + (x + x')^2 + (z + z')^2} \approx D_1 + \frac{(x + x')^2 + (z + z')^2}{2D_1} \tag{18}$$

in which the following condition needs to be satisfied

$$\frac{(x + x')^2 + (z + z')^2}{D_1^2} \ll 1. \tag{19}$$

Note that (19) is valid as a result of (13). Similarly, we also have

$$\sqrt{D_2^2 + (x + x')^2 + (z + z')^2} \approx D_2 + \frac{(x + x')^2 + (z + z')^2}{2D_2}, \tag{20}$$

Consequently, FSSR is given as follows:

$$\varepsilon \approx \left|1 + \frac{(D_1 + D_2)\,i}{D_1 D_2} \iint F\left(x', z'\right) e^{\frac{D_1+D_2}{D_1 D_2}\pi i[(x+x')^2+(z+z')^2]} dx' dz'\right|^2 \tag{21}$$

Let R defined as (1), (21) then becomes

$$\varepsilon \approx \left|1 + \frac{i}{R} \iint F\left(x', z'\right) e^{\frac{\pi i}{R}[(x+x')^2+(z+z')^2]} dx' dz'\right|^2, \tag{22}$$

which is exactly the same as (10).

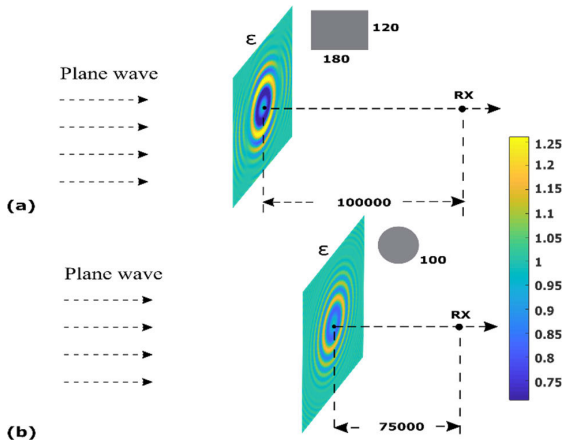

FIGURE 4. The plane wave equivalent models for the FSR systems in Fig. 2 and the numerically calculated FSSRs for a plane perpendicular to the direction of propagation.

The analysis above indicates that the FSSR model based on the Kirchhoff diffraction formula can be approximated as a plane wave equivalent model, which is based on the Fresnel diffraction formula. The equivalent model is premised on the assumption that both the target's dimension and its distance from the baseline are significantly less than its distances to the transmitter and the receiver. This assumption is considered valid for most FSR applications. A system with a point source can be regarded equivalently as a system with a plane wave, where the distance between the target and the receiver is given by (1). The plane wave equivalent model for the setups in Fig. 2 and the numerically calculated FSSRs using (22) are show in Fig. 4. Compared with Fig.2, it can be seen that the FSSRs are essentially the same.

B. NUMERCIAL RESULTS OF PLANE WAVE EQUIVALENCE FOR TARGET CROSSING THE BASELINE

Consider the far-field parameter S [14]:

$$S = \frac{2H^2}{D}, \tag{23}$$

in which H is the largest dimension (normalized with respect to the wavelength) of the target.

In Fig. 5, we assume that the target is travelling perpendicularly crossing the baseline in the z direction and examine the FSSR calculated by the Kirchhoff diffraction given by (2) to (8) and the FSSR given by the equivalent model in (22). The distances of D_1 and D_2 are set at 3×10^5 and 10^5, respectively, so R in the equivalent model is 7.5×10^4 according to (1). The target in Fig. 5(a) is a circle with a diameter of 100, so it is a far-field scenario with $S = 0.2$. Both the FSSR by the Kirchhoff diffraction (ε_K) and that given by the equivalent model (ε_F) are represented by the same black curve as they cannot be visually distinguished from each other. The difference between them ($\varepsilon_K - \varepsilon_F$) is plotted with the red dashed curve. It can be seen that the difference between ε_K and ε_F is in the order of 10^{-4}. In Fig. 5(b), the target is a circle with a diameter of 200 so it is a close to near-field scenario where $S = 0.8$. Compare to (a), the ranges

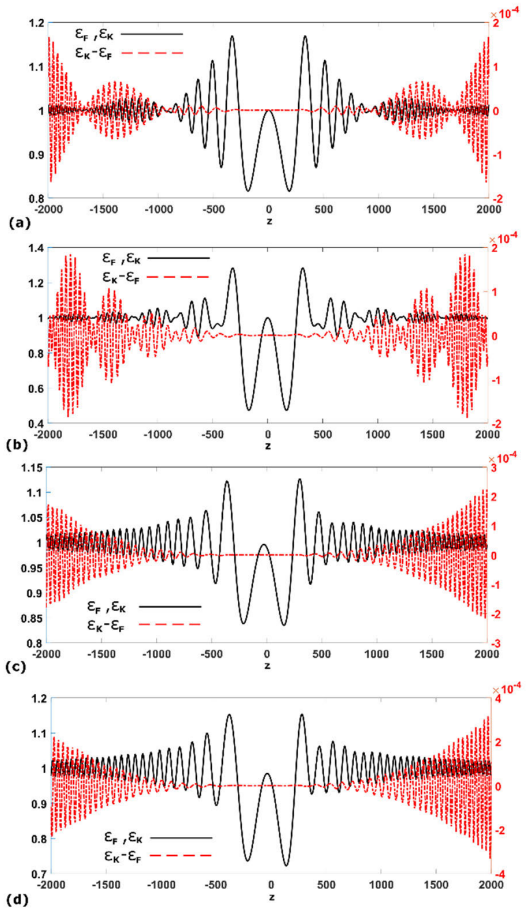

FIGURE 5. The difference between the FSSR calculated in the point source model by the Kirchhoff diffraction formula and that in the plane wave equivalent model by the Fresnel diffraction formula. (a) The target is a circle with a diameter of 100. (b) A circle with a diameter of 200. (c) An isosceles triangle with base 100 and height 150. (d) An isosceles triangle with base 140 and height 210.

of ε_K and ε_F are larger due to stronger shadowing effects, but the difference between them is still in the order of 10^{-4}. Fig. 5(c) shows the results of an isosceles triangle target with base 100 (along the x direction) and height 150 ($S = 0.45$), and Fig. 5(d) is for a similar triangle with base 140 and height 210 ($S = 0.88$). It can be concluded that the plane wave equivalent model generates very marginal errors for both the far-field and the close to near-field scenarios. The errors are generally larger when the target is farther away from the base line, which can be explained by the condition in (13).

IV. SHADOW PROFILE RETRIEVAL USING PLANE WAVE EQUIVALENT MODEL

A. OPTIMIZATION METHOD

Here we briefly describe the optimization method for the model illustrated in Fig. 3. Different from [1] and [2], FSSR here is a function of the x and z coordinates of the target, rather than the coordinates of the receiver. As in [1] and [2], we divide the target shadow into N strips with equal width and each individual strip p is regarded as a rectangle (Fig. 6

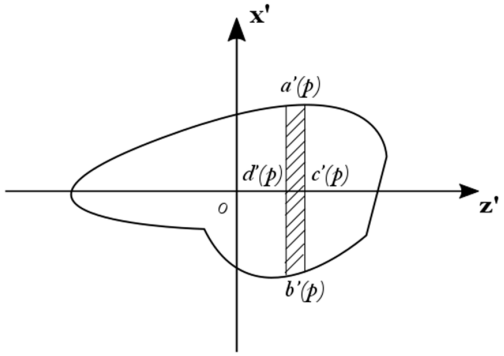

FIGURE 6. The target shadow is divided into strips, one of which is shown by the shaded area. Each strip is regarded as a rectangle.

for illustration). From (22), we then define

$$A_F(x,z) = \iint F(x',z')\, e^{\frac{\pi i}{R}[(x+x')^2+(z+z')^2]} dx'dz'. \quad (24)$$

Considering all the strips, the integration in (24) can be approximated as

$$A_F(x,z) \approx \sum_{p=1}^{N} f(a'_p, b'_p, x) G_p(z), \quad (25)$$

where a'_p and b'_p are the upper and lower limits of strip p, respectively, and $f(a'_p, b'_p, x)$ is given by

$$f(a'_p, b'_p, x) = \int_{b'_p}^{a'_p} e^{\frac{\pi i}{R}(x+x')^2} dx'$$
$$= \sqrt{\frac{R}{4i}}\left(\mathrm{erfi}\left(\sqrt{\frac{i\pi}{R}}(a'_p + x)\right) - \mathrm{erfi}\left(\sqrt{\frac{i\pi}{R}}(b'_p + x)\right)\right), \quad (26)$$

and $G_p(z)$ is given by

$$G_p(z) = \int_{d'_p}^{c'_p} e^{\frac{\pi i}{R}(z'+z)^2} dz'$$
$$= \sqrt{\frac{R}{4i}}\left(\mathrm{erfi}\left(\sqrt{\frac{i\pi}{R}}(c'_p + z)\right) - \mathrm{erfi}\left(\sqrt{\frac{i\pi}{R}}(d'_p + z)\right)\right), \quad (27)$$

in which c'_p and d'_p respectively mark the z' coordinates of the right and left limits of strip p. Note that in this retrieval method, the location of the target is assumed known and the width of the strips are predefined, so c'_p, d'_p and z are considered known. In (26) and (27), erfi (x) is the imaginary error function [15].

Let

$$a_p = a'_p + x, \quad (28)$$

and

$$b_p = b'_p + x. \quad (29)$$

Equations (25) and (26) then become

$$A_F(z) \approx \sum_{p=1}^{N} f(a_p, b_p) G_p(z), \tag{30}$$

and

$$f(a_p, b_p) = \sqrt{\frac{R}{4i}} \left(\text{erfi}\left(\sqrt{\frac{i\pi}{R}} a_p \right) - \text{erfi}\left(\sqrt{\frac{i\pi}{R}} b_p \right) \right). \tag{31}$$

Equation (22) then becomes

$$\varepsilon(x, z) = \left| 1 + \frac{i}{R} \sum_{p=1}^{N} f(a_p, b_p) G_p(z) \right|^2. \tag{32}$$

Suppose that there are M observations of the FSSR, each is denoted by ε_q for the target at $(x_q, 0, z_q)$, $q = 1, \cdots, M$, solving (a_p, b_p) can then be formulated as a nonlinear least-square problem:

$$\left(\hat{a}_p, \hat{b}_p\right) = \arg\min \sum_{q=1}^{M} r_q^2 \tag{33}$$

where

$$r_q = \varepsilon_q - \left| 1 - \frac{1}{iR} \sum_{p=1}^{N} f(a_p, b_p) G_p(z_q) \right|^2. \tag{34}$$

By solving (33), the optimal values for (a_p, b_p) can be calculated and thus the shadow profile of the target is retrieved. Note that a_p and b_p are respectively the x coordinates of the upper and lower limits of strip p. Hence, it is convenient to graph the retrieved shape on the $x - z$ plane.

B. RETRIEVAL WITH ONE RECEIVER

We use the forward scatter radar setup illustrated in Fig. 1 to numerically examine the retrieval of target shadow profile via the plane wave equivalent model. The distances of D_1 and D_2 are fixed at 3×10^5 and 10^5, respectively, while targets of various sizes and shapes are tested to cover both the far-field and the close to near-field scenarios. Since for any 3D shapes only the shadow silhouette plays a part in the FSSR, in our analysis we assume that all targets are 2D and located on a plane ($x' - z'$ plane in Figs. 1 and 3). The targets all move on the plane perpendicular to the y-axis and in the direction of the z-axis. The true FSSR is calculated using (2), (3) and (8).

The shadow profile retrieval is achieved by solving the optimization problem (34), where R is calculated using (1) from D_1 and D_2 (R is 7.5×10^4 in this case). We also assume that a sufficient number of FSSR samples are available without any errors. As shown in our previous work [3], the minimum value of the FSSR can provide a good estimation of the size of the target. For instance, a minimum value of 0.8 in the FSSR samples corresponds to a circular target with an approximate diameter of 100 for $R = 7.5 \times 10^4$. We quadruple this dimension and uses $z = -200$ to $z = 200$ on the $x - z$ plane as the target retrieval range. The number of strips covering this range is then set to 40

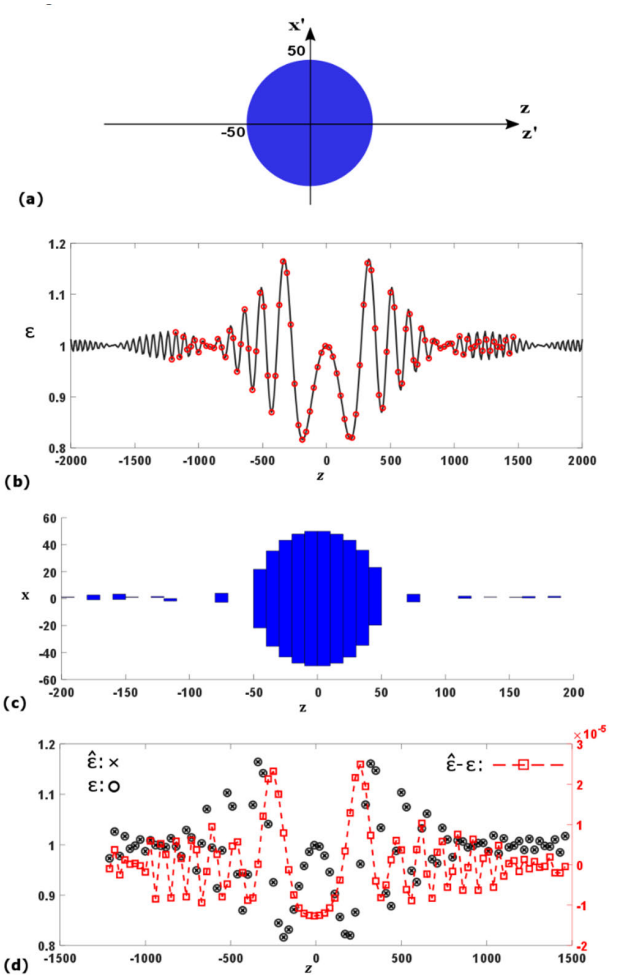

FIGURE 7. (a) Dimensions and location of the circular target. (b) The true FSSR is shown by the black curve, and the 90 FSSR samples when the target is moving in the z direction are marked by the red circles. (c) The retrieved shadow profile through the plane wave equivalent model. (d) The sampled FSSR (black circles), the recalculated FSSR (black crosses) using the retrieved shape and their difference (red squares).

(strip width is 10) so all c'_p and d'_p are known. The nonlinear least-square function ('lsqnonlin' in MATLAB) with the trust-region-reflective algorithm [16] is used to solve the optimization problem. Once the estimated limits $(\hat{a}_p, \hat{b}_p)$ for the strips are ready, we mark the location of each strip on the $x-z$ plane only if $\hat{a}_p > \hat{b}_p$. The strip is considered nonexistent if $\hat{a}_p < \hat{b}_p$.

The first target we use is a circle with a diameter of 100 (Fig. 7(a)). It moves along the line of $x = 0$, so the projection of the z-axis on the $x' - z'$ plane overlaps with the z'-axis (see Fig. 7(a)). The true values of the FSSR when the target is moving are shown by the black curve in Fig. 7(b). We take a finite number of samples of the FSSR to retrieve the shadow profile of the target. In this case, 90 samples (shown by the red circles in Fig. 7(b)) with a fixed increment in the z-axis are selected.

The final retrieved target shadow profile is shown in Fig. 7(c), which shows a high level of agreement with the true target shape. We also plot the sampled FSSR (ε), the

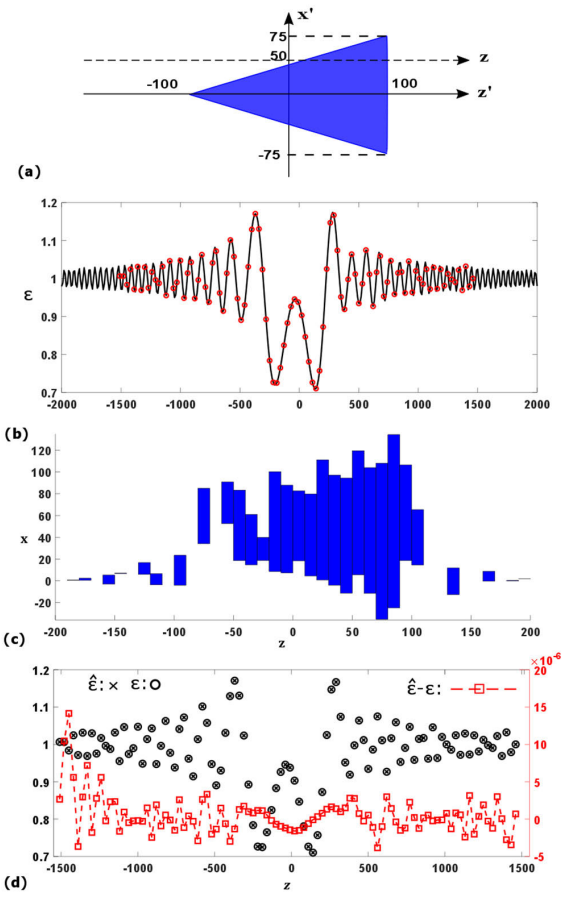

FIGURE 8. (a) Dimensions and location of the triangular target. (b) The true FSSR is shown by the black curve, and the 100 FSSR samples when the target is moving in the z direction are marked by the red circles. (c) The retrieved shadow profile through the plane wave equivalent model. (d) The sampled FSSR (black circles), the recalculated FSSR (black crosses) using the retrieved shape and their difference (red squares).

recalculated FSSR ($\hat{\varepsilon}$) using (35), and their difference for the 90 samples in Fig. 7(d). It can be seen that the difference between the FSSRs generated by the true and the retrieved shadow profiles is in the order of 10^{-5}.

$$\hat{\varepsilon}_q = \left|1 - \frac{1}{iR}\sum_{p=1}^{40} f(\hat{a}_p, \hat{b}_p) G_p(z_q)\right|^2. \tag{35}$$

The second target is a triangle shown in Fig. 8(a), whose geometric center moves along the line of $x = -50$. As a result, the projection of the z-axis on the $x' - z'$ plane is at $x' = 50$, shown by the dashed axis in Fig. 8(a). The dimensions of the triangle suggest that the far-field parameter S is 0.8, i.e., it is a close to near-field scenario. The true FSSR is shown by the back curve and the 100 samples used for retrieval are marked by the red circles in Fig. 8(b).

The retrieved shape represented by the strips is shown in Fig. 8(c), from which we can see that although the retrieved strips do display a triangular shape, their center is approximately on the line of $x = 50$ while the correct position should be at $x = -50$. This is because of the inherent ambiguity induced by observing the FSSR from one receiver. From Fig. 1, we can see that the observed FSSRs are exactly

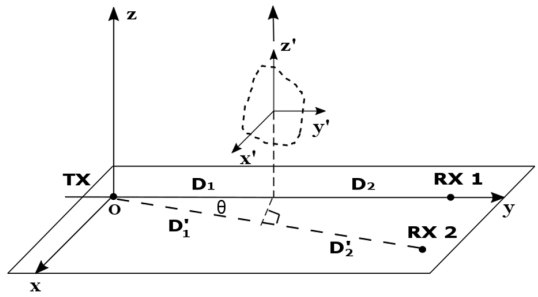

FIGURE 9. An illustration of the forward scatter system where two receivers are used.

the same if the target is moving along $x = \mathrm{A}$ and $x = -\mathrm{A}$. In Fig. 8(d), it can be seen that the difference between $\hat{\varepsilon}$ and ε is still very small for the triangular target.

C. RETRIEVAL WITH TWO RECEIVERS

The ambiguity in the retrieval can be eliminated when two receivers are used. Here we consider a system with one transmitter and two receivers illustrated in Fig. 9. The two receivers are located on the $x - y$ plane and their lines of sight towards the transmitter have a small angle of θ. The target's projection on the baseline of the second receiver has a distance of D'_1 from the transmitter and D'_2 from the second receiver. When the target is moving in the direction of the z-axis, the movement is always perpendicular to both baselines. As a result, D'_1 is given by

$$D'_1 = D_1 \cos\theta. \tag{36}$$

The second receiver provides us with a second plane equivalent model where

$$R' = \frac{D'_1 D'_2}{D'_1 + D'_2}. \tag{37}$$

As angle θ is very small, we can assume that the target has the same shadow profile from the two different look angles provided by the two receivers. If the upper and lower limits for a strip are (a_p, b_p) for the first plane wave equivalent model with the first receiver, the upper and lower limits for the second model with the second receiver are given by

$$a_p^* = a_p - D_1 \sin\theta, \tag{38}$$

and

$$b_p^* = b_p - D_1 \sin\theta. \tag{39}$$

With the relation between (a_p, b_p) and (a_p^*, b_p^*) established by (38) and (39), the two plane wave equivalent models are joined together to form a single least-squares problem of (33) to optimize $(\hat{a}_p, \hat{b}_p)$.

In the following analysis, the second receiver is placed on the $x - y$ plane with a distance 500 from the first receiver. The two receivers have equal distances from the transmitter. Again, the true FSSR is calculated using (2), (3) and (8). The samples of the FSSR from the two receivers are used to retrieve the upper and lower limits of the strips. In Fig. 10, the retrieval for the same target in Fig. 8(a) is shown. The true

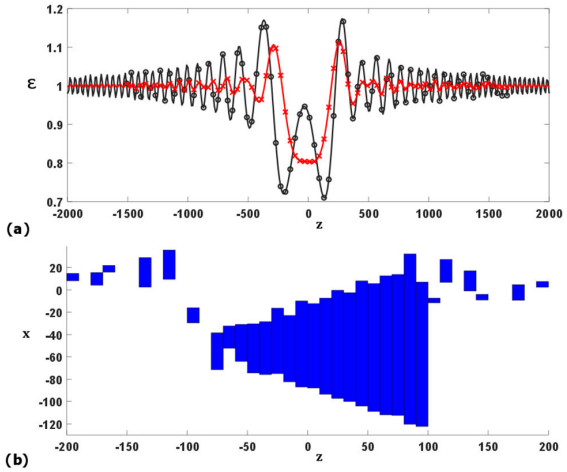

FIGURE 10. (a) The true FSSRs for the first and second receivers are shown by the black and red curves, respectively. The samples used for retrieval are marked by the black circles (the first receiver) and the red crosses (the second receiver). (b) The retrieved shadow profile using two receivers.

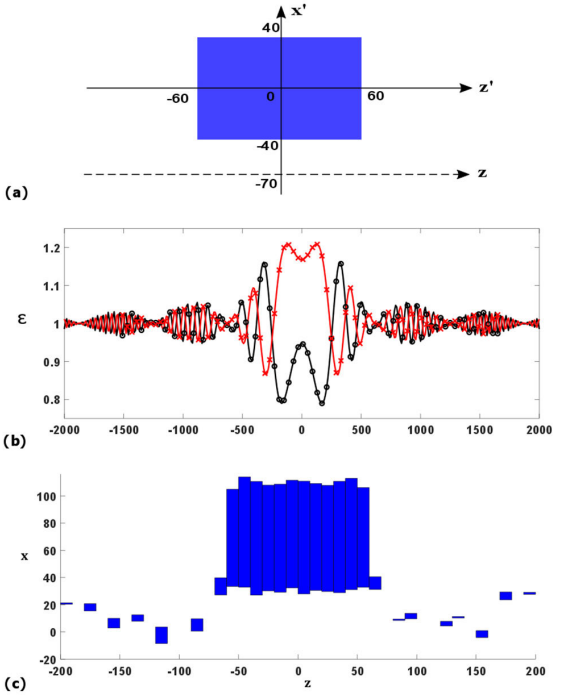

FIGURE 11. (a) Dimensions and location of the rectangular target. (b) The true FSSRs for the first and second receivers are shown by the black and red curves, respectively. The samples used for retrieval are marked by the black circles (the first receiver) and the red crosses (the second receiver). (c) The retrieved shadow profile using two receivers.

FSSR of the first receiver is denoted by the black curve with 80 samples marked by the black circles in Fig. 10(a). For the second receiver, the true FSSR is given by the red curve with 80 samples marked by the red crosses. The retrieval outcome is shown in Fig. 10(b). Compared to Fig. 8(c), it can be seen that the additional receiver not only corrects the position of the target but also improves the accuracy of the shadow profile retrieval.

Two more targets are used to verify the performance of the retrieval with two receivers. The first target is a rectangle with

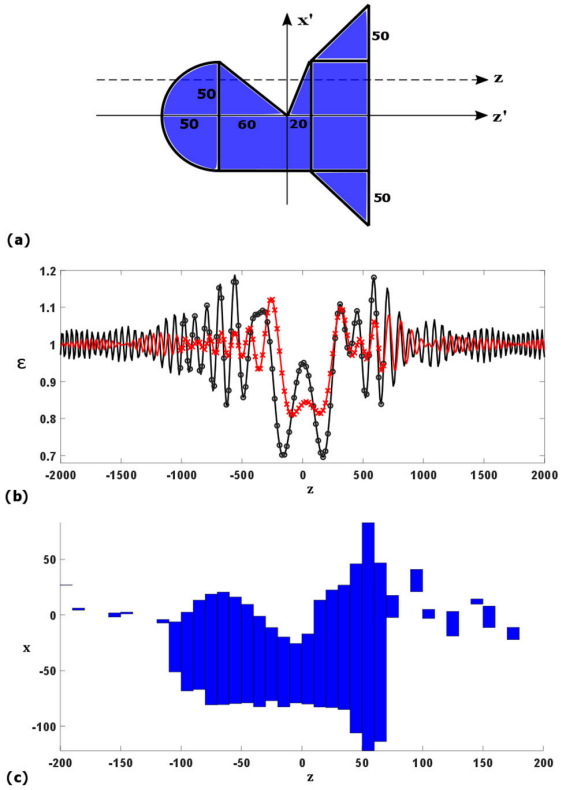

FIGURE 12. (a) Dimensions and location of the irregular target. (b) The true FSSRs for the first and second receivers are shown by the black and red curves, respectively. The samples used for retrieval are marked by the black circles (the first receiver) and the red crosses (the second receiver). (c) The retrieved shadow profile using two receivers.

dimensions shown in Fig. 11(a). Its geometric center moves along the line of $x = 70$, so the projection of the z-axis on the $x' - z'$ plane is at $x' = -70$. In Fig. 11(b), the true and sampled FSSRs from the two receivers are shown in the same way as before. The retrieved target shadow profile is shown in Fig. 11(c). The second target has an irregular shape with dimensions shown in Fig. 12(a). Its geometric center moves along the line of $x = -30$, so the projection of the z-axis on the $x' - z'$ plane is at $x' = 30$. The true and sampled FSSRs are shown Fig. 12(b), and the retrieved target shadow profile is shown in Fig. 12(c). From Figs. 11 and 12, we can see that the retrieved shadow profiles using the FSR system with two receivers display a high level of agreement with the true shadow profiles.

V. CONCLUSION

In this paper, we present an analysis of the forward scatter shadow ratio using a spherical wave model and the Kirchhoff diffraction formula. Aiming to overcome the limitations of previous studies, we build an FSR system model in which the transmitter is regarded as a point source and the target is moving across the transmitter-receiver baseline. A comparison between the new point source model and the existing model based on the Fresnel formula is given, and a plane wave equivalent model for the new model is derived. Using numerical analysis, it is shown that the plane wave equivalent

model generates very marginal errors for both the far-field and the close to near-field scenarios.

The optimization method for target shadow profile retrieval is discussed within the framework of the new model. In this approach, the target shadow profile, represented as a finite set of rectangular strips, is retrieved using discrete samples of the FSSR. The plane wave equivalent model is applied to enable the utilization of the nonlinear least-squares algorithm to optimize both the upper and lower limits of the strips. Different targets with various sizes and shapes are used to evaluate the shadow profile retrieval capability of the proposed method under both far-field and close to near-field scenarios. It is suggested that incorporating two receivers, as opposed to just one, aids in resolving the ambiguity associated with target localization and enhances the precision of target shadow profile retrieval.

REFERENCES

[1] X. Shen and D. D. Huang, "An optimization method for shadow profile retrieval with forward scatter shadow ratio," in *Proc. Int. Symp. Commun. Inf. Technol.*, Sydney, NSW, Australia, Oct. 2023.
[2] X. Shen and D. Huang, "Forward scatter shadow ratio: Concept and its application in shadow profile retrieval," *IEEE Access*, vol. 11, pp. 77147–77162, 2023, doi: 10.1109/ACCESS.2023.3298107.
[3] X. Shen and D. D. Huang, "Forward scatter shadow ratio for passive forward scatter radar," in *Proc. Int. Symp. Antennas Propag. (ISAP)*, Oct. 2022, pp. 39–40, doi: 10.1109/ISAP53582.2022.9998598.
[4] J. I. Glaser, "Bistatic RCS of complex objects near forward scatter," *IEEE Trans. Aerosp. Electron. Syst.*, vol. AES-21, no. 1, pp. 70–78, Jan. 1985, doi: 10.1109/TAES.1985.310540.
[5] A. B. Blyakhman and I. A. Runova, "Forward scattering radiolocation bistatic RCS and target detection," in *Proc. IEEE Radar Conf. Radar Next Millennium*, Apr. 1999, pp. 203–208, doi: 10.1109/NRC.1999.767314.
[6] I. Suberviola, I. Mayordomo, and J. Mendizabal, "Experimental results of air target detection with a GPS forward-scattering radar," *IEEE Geosci. Remote Sens. Lett.*, vol. 9, no. 1, pp. 47–51, Jan. 2012, doi: 10.1109/LGRS.2011.2159477.
[7] R. S. A. R. Abdullah, S. A. Musa, N. E. A. Rashid, A. Sali, A. A. Salah, and A. Ismail, "Passive forward-scattering radar using digital video broadcasting satellite signal for drone detection," *Remote Sens.*, vol. 12, no. 18, p. 3075, Sep. 2020. [Online]. Available: https://www.mdpi.com/2072-4292/12/18/3075
[8] F. Colone, T. Martelli, and P. Lombardo, "Quasi-monostatic versus near forward scatter geometry in WiFi-based passive radar sensors," *IEEE Sensors J.*, vol. 17, no. 15, pp. 4757–4772, Aug. 2017, doi: 10.1109/JSEN.2017.2713450.
[9] V. V. Chapurskiy and V. N. Sablin, "SISAR: Shadow inverse synthetic aperture radiolocation," in *Proc. Rec. IEEE Int. Radar Conf.*, May 2000, pp. 322–328, doi: 10.1109/RADAR.2000.851854.
[10] J. W. Goodman, *Introduction to Fourier Optics*. New York, NY, USA: McGraw-Hill, ch. 10, 1996.
[11] C. Hu, L. Wang, and C. Liu, "SISAR imaging method based on GNSS signal: Theory and experimental results," in *Proc. CIE Int. Conf. Radar (RADAR)*, Oct. 2016, pp. 1–5, doi: 10.1109/RADAR.2016.8059223.
[12] D. Olivadese, E. Giusti, D. Petri, M. Martorella, A. Capria, and F. Berizzi, "Passive ISAR with DVB-T signals," *IEEE Trans. Geosci. Remote Sens.*, vol. 51, no. 8, pp. 4508–4517, Aug. 2013, doi: 10.1109/TGRS.2012.2236339.
[13] I. Theodorou, C. V. Ilioudis, C. Clemente, and M. Vasile, "SISAR imaging—Radio holography signal reconstruction based on receiver-transmitter motion," in *Proc. IEEE Radar Conf. (RadarConf)*, Apr. 2019, pp. 1–6, doi: 10.1109/RADAR.2019.8835596.
[14] N. Ustalli, P. Lombardo, and D. Pastina, "Detection performance of a forward scatter radar using a crystal video detector," *IEEE Trans. Aerosp. Electron. Syst.*, vol. 54, no. 3, pp. 1093–1114, Jun. 2018, doi: 10.1109/TAES.2017.2774659.
[15] L. C. Andrews, *Special Functions of Mathematics for Engineers*, 2nd ed. Oxford, U.K.: Oxford Univ. Press, 1997.
[16] T. F. Coleman and Y. Li, "An interior trust region approach for nonlinear minimization subject to bounds," *SIAM J. Optim.*, vol. 6, no. 2, pp. 418–445, May 1996, doi: 10.1137/0806023.

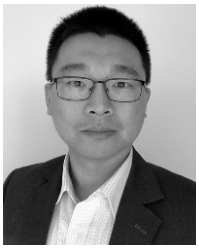

XI SHEN (Member, IEEE) received the B.E.E.E. degree in electronic engineering from Tsinghua University, Beijing, China, in 2003, and the Ph.D. degree in electronic engineering from the Imperial College London, London, U.K., in 2006.

He was with China Unicom as a Telecommunication Engineer and then a Senior Engineer for eight years. He is currently a Research Associate with the School of Electrical, Electronic, and Computer Engineering, The University of Western Australia, Perth, Australia. His research interests include environmental monitoring using microwave communication links, signal processing in satellite communication, and forward scatter radar.

DEFENG (DAVID) HUANG (Senior Member, IEEE) received the B.E.E.E. and M.E.E.E. degrees in electronic engineering from Tsinghua University, Beijing, China, in 1996 and 1999, respectively, and the Ph.D. degree in electrical and electronic engineering from The Hong Kong University of Science and Technology (HKUST), Hong Kong, in 2004.

Before joining The University of Western Australia (UWA), he was a Lecturer with Tsinghua University. In 2005, he joined the School of Electrical, Electronic and Computer Engineering, UWA, as a Lecturer, where he has been promoted to be a Professor, since 2011. He served as an Editor for the IEEE TRANSACTIONS ON WIRELESS COMMUNICATIONS and the IEEE WIRELESS COMMUNICATIONS LETTERS, from 2005 to 2011 and from 2011 to 2015, respectively, and an Editorial Assistant for the IEEE TRANSACTIONS ON WIRELESS COMMUNICATIONS, from 2002 to 2004.